



Particles II

Access the latest eBook →

11

Advanced
Optical Metrology

Particles II



EVIDENT
OLYMPUS

WILEY

Impact on Biological Systems and the Environment

This eBook is dedicated to the research of Professor David Wertheim. In collaboration with various groups, Professor Wertheim uses confocal microscopy to analyse the impact of different types of particles on human health and the environment, with a focus on human health-hazardous particles detected with solid-state nuclear track detectors (SSNTD). Download for free, today.

EVIDENT
OLYMPUS

WILEY

Oxygen Vacancy-Rich $\text{La}_{0.5}\text{Sr}_{1.5}\text{Ni}_{0.9}\text{Cu}_{0.1}\text{O}_{4-\delta}$ as a High-Performance Bifunctional Catalyst for Symmetric Ammonia Electrolyzer

Mengfei Zhang, Peimiao Zou, Georgina Jeerh, Boyao Sun, Marc Walker, and Shanwen Tao*

In this study, strontium and copper dual-doped La_2NiO_4 annealed in Ar ($\text{La}_{0.5}\text{Sr}_{1.5}\text{Ni}_{0.9}\text{Cu}_{0.1}\text{O}_{4-\delta}$ -Ar, LSNC-Ar) with K_2NiF_4 structure is strategically designed as an ammonia oxidation reaction (AOR) and hydrogen evolution reaction (HER) bifunctional catalyst for high-efficiency ammonia electrolysis. The selective substitution of lanthanum with high content strontium improves the electronic conductivity and increases the oxygen vacancy concentration. Doping of Cu into the B-site of the perovskite induces a synergistic interplay of Ni and Cu, leading to excellent AOR activity. Due to the excellent AOR and HER activity of doped La_2NiO_4 , a symmetric ammonia electrolyzer based on LSNC-Ar (SAE-LSNC-Ar) is assembled and investigated for the removal of ammonia. In addition, the performance of the SAE is comparable to the ammonia electrolyzer based on a PtIr/C anode and Pt/C cathode at low voltage. This is the first report using an oxide with the K_2NiF_4 structure as an efficient AOR catalyst. The assembled SAE-LSNC-Ar shows $\approx 95\%$ ammonia removal efficiency in real landfill leachate, which is the highest among electrochemical removal of ammonia in landfill leachate. This study paves an attractive route to explore materials with the K_2NiF_4 structure as highly efficient AOR/HER bifunctional catalysts for the electrolysis of ammonia.

recognized as a sustainable low carbon fuel.^[1] At present, there has been great attention on the importance of ammonia regarding everyday life and production, and as a result, the concept of ammonia economy has gained much interest over the past ten years.^[2] Although ammonia is important to our society, the potential environmental impacts caused by the increased use of ammonia must be considered.^[2] The main source of toxic ammonia is from agriculture.^[3] As ammonia is extremely soluble in water, e.g., 308 g of ammonia per liter of aqueous solution, residual ammonia is always dissolved in water and subsequently discharges into wastewater. Even if the ammonia content is quite low, it still has significantly negative effects on both the natural environment and human health.^[4] Therefore, the removal of ammonia from wastewater is an important research topic for wastewater treatment.^[5]

1. Introduction

For decades ammonia has been considered a globally vital commodity for fertilizer production and has increasingly been

Although a variety of techniques such as microbial, physical and chemical processes have been studied for the removal of ammonia, electro-oxidation of ammonia is an environmentally benign technology that can be well controlled by electrical power input.^[6] Electro-oxidation of ammonia is normally achieved by ammonia electrolysis, which composes of ammonia oxidation reaction (AOR) at the anode side and hydrogen evolution reaction (HER) at the cathode side.^[7] In recent years, researchers have done a lot of work on electro-oxidation of ammonia, but there remains significant gaps before this technology can be adopted by broader industrial applications. This is mainly due to concerns over economic feasibility and technical drawbacks.^[6a] A grand challenge is to develop highly active precious-metal-free catalysts for ammonia oxidation in order to reduce the cost of electrolyzers. Pt-based catalysts are most investigated and PtIr/C has proven to be the best AOR catalyst up to now due to its ability to activate and to make new bonds.^[8] However, the large-scale application of expensive precious metals, e.g. Pt and Ir, in wastewater treatment is not realistic in terms of economic consideration. Low-cost and highly active catalyst is subsequently in high demand for the electrolysis of ammonia.^[6d,9] Another challenge for practical applications is low efficiency associated with poor stability in real wastewater. Although high removal of ammonia by electro-oxidation has been reported in some papers, most of these works

M. F. Zhang, P. M. Zou, G. Jeerh, B. Y. Sun, S. W. Tao
School of Engineering
University of Warwick
Coventry CV4 7AL, UK
E-mail: s.tao.1@warwick.ac.uk

M. Walker
Department of Physics
University of Warwick
Coventry CV4 7AL, UK

S. W. Tao
Department of Chemical Engineering
Monash University
Clayton, Victoria 3800, Australia

 The ORCID identification number(s) for the author(s) of this article can be found under <https://doi.org/10.1002/adfm.202204881>.

© 2022 The Authors. Advanced Functional Materials published by Wiley-VCH GmbH. This is an open access article under the terms of the Creative Commons Attribution License, which permits use, distribution and reproduction in any medium, provided the original work is properly cited.

DOI: 10.1002/adfm.202204881

focus on synthetic wastewater.^[10] The performance always tends to suffer a sharp drop when it comes to real wastewater, due to the instability of the electrode and the complex solution environment. Improving the performance and stability of the catalysts in real wastewater paves the way for large-scale applications.

Due to the tunable electronic structures and flexible compositions of perovskites, we recently reported a precious-metal-free and bifunctional perovskite catalyst for ammonia electrolysis.^[6d] The assembled symmetric ammonia electrolyzer (SAE) based on Cu-doped LaNiO_3 benefited from oxygen vacancies and the synergistic effect of different active sites in the B-site. Consequently, the system had the ability to remove almost all ammonia in an alkaline solution. However, in real landfill leachate, the ammonia removal efficiency of the SAE declined to $\approx 70\%$. It is believed that insufficient stability and activity of the simple perovskite catalyst in extreme environments affects its practical use. It has been demonstrated that oxygen vacancies play a vital role in the ammonia oxidation process.^[6d,11] In order to further improve ammonia removal efficiency, it is anticipated that increasing the oxygen vacancy concentration may lead to elevated AOR activity and subsequently enhance ammonia removal efficiencies. One of the most common ways to create defects in perovskite oxides is partially substituting the A-site (e.g., La) with low-valent cations, such as Sr.^[12] Unfortunately, partially replacing La^{3+} in this perovskite by Sr^{2+} ions at high level leads to phase segregation and decreased catalytic activity.^[13]

In order to obtain high oxygen vacancy catalyst and avoid the formation of impurities, we investigate an alternative Ruddlesden-Popper (RP) oxide. The RP-type oxide is a promising candidate for electrochemical catalysis due to its wide element accommodation, tunable electronic structure and controllable stoichiometry.^[14] RP oxides have a general formula of $\text{A}_{n+1}\text{B}_n\text{O}_{3n+1}$ or equivalently $(\text{AO})(\text{ABO}_3)_n$, where n is the number of perovskite layers. RP phase with a single perovskite layer is the most widely studied structure and is also referred to as the K_2NiF_4 structure. **Figure 1a** shows the schematic diagram of the crystal structure, where the A-site is larger than that of the B-site cation.^[15] For La_2NiO_4 , the single LaNiO_3 perovskite layer is stacked between the LaO rock-salt layer along the crystallographic c -axis. Since the A-site cation elongates the interlayer distance, the RP structure is able to accommodate most elemental substitutions as well as additional compositions which are not as stable.^[16] For example, it is known that the solid solubility of Sr in LaNiO_3 is limited to $\approx 5\text{--}20\%$, but 75% La can be occupied by Sr in La_2NiO_4 to form stable $\text{La}_{0.5}\text{Sr}_{1.5}\text{NiO}_4$.^[17] Despite there is an debate about whether the low concentration Sr doping La_2NiO_4 is oxygen excess or oxygen deficiency, it is clear that when reaching a Sr-substitution of over 50%, $\text{La}_{2-x}\text{Sr}_x\text{NiO}_4$ is in a high oxygen-deficient regime and the vacancy concentration increases with the increased content of Sr.^[18] Due to the flexible properties of this structure, RP oxides have been applied in various catalytic reactions, such

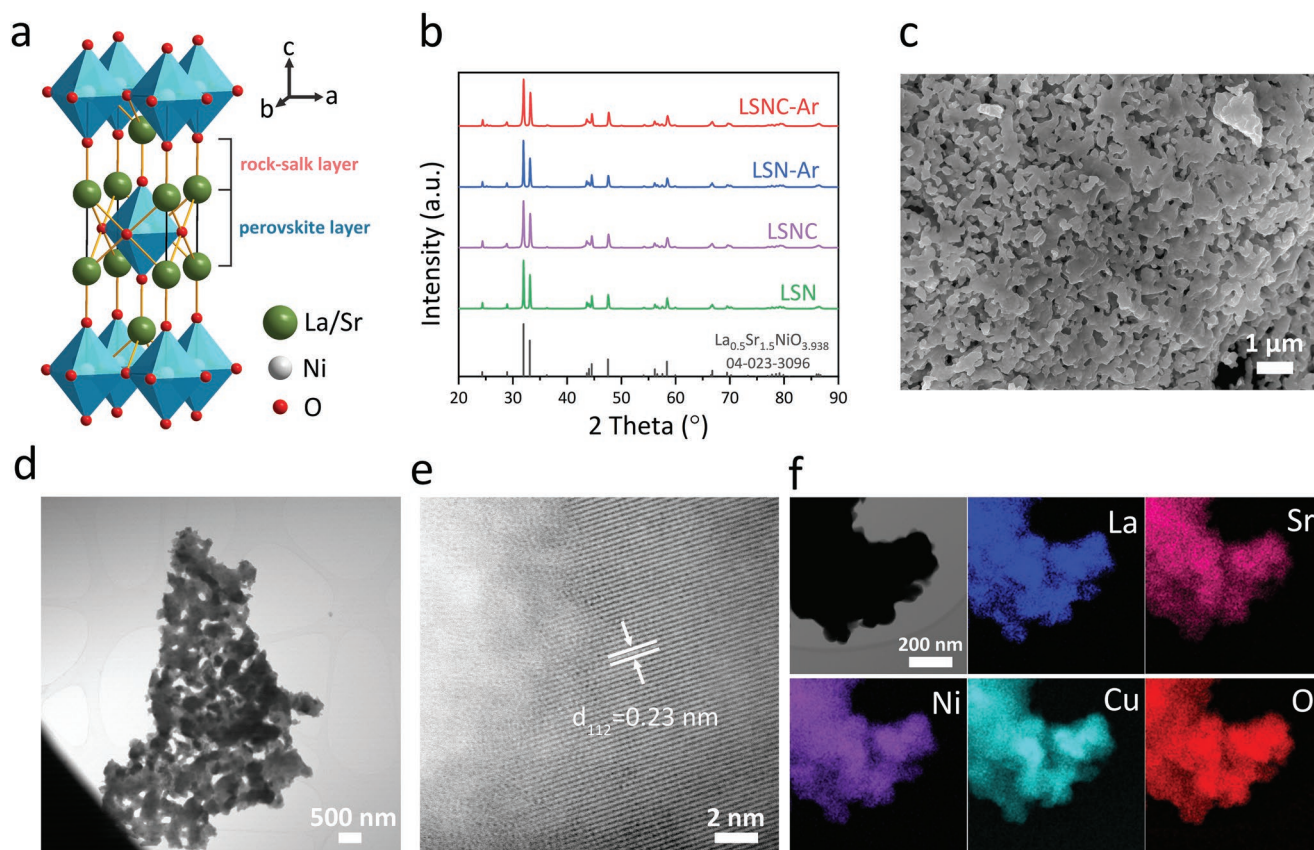


Figure 1. Structure. a) Schematic diagram of the RP-type oxide crystal structure. b) XRD patterns of $\text{La}_{0.5}\text{Sr}_{1.5}\text{NiO}_{3.938}$ standard card (ICDD: 04-023-3096), LSN, LSN-C, LSN-Ar and LSN-C-Ar. c) SEM image, d) TEM image and e) HRTEM image of LSN-C-Ar. f) HAAD-STEM image and corresponding EDS elemental mappings of La, Sr, Ni, Cu, and O.

as the oxygen reduction reaction (ORR),^[19] oxygen evolution reaction (OER),^[20] and urea oxidation reaction (UOR).^[13a] However, to the best of our knowledge, there is no report on using oxides with this structure as AOR catalysts. According to the previous work, the highest reported doping concentration of Sr in La_2NiO_4 is 75%. In order to obtain a high oxygen vacancy, a 75% Sr doped La_2NiO_4 ($\text{La}_{0.5}\text{Sr}_{1.5}\text{NiO}_{4-\delta}$, LSN) was chosen as the patent phase in this study. Another advantage of the high Sr content in RP oxides is the excellent mixed ionic-electronic conducting properties.^[14b,21] It is known that >50% Sr substitution for La induces semiconducting or metallic-type behavior in La_2NiO_4 due to hole doping in the O 2p band, while doping La_2NiO_4 with other alkaline-earth ions has little influence on electrical conductivity.^[20,22] High electrical conductivity of the catalyst induces better electrocatalytic performance since catalytic reactions involve the transfer of electrons.^[12]

In this work, we demonstrated an excellent bifunctional catalyst, $\text{La}_{0.5}\text{Sr}_{1.5}\text{Ni}_{0.9}\text{Cu}_{0.1}\text{O}_{4-\delta}$ -Ar (LSNC-Ar). In comparison with the previous study,^[6d] the improvements of this work are: 1) Benefiting from the flexible properties of RP structure, the oxygen-vacancy-enrichment and high conductivity of LSNC-Ar was prepared. To the best of our knowledge, this is the first report using an oxide with the K_2NiF_4 structure for AOR catalysts, which also exhibits excellent HER activity. 2) A highly efficient SAE was assembled based on the LSNC-Ar catalyst and it showed $\approx 95\%$ ammonia removal in real wastewater. Additionally, the SAE exhibits the highest ammonia removal efficiency in landfill leachate to date. The superior ammonia removal efficiency combined with the design and synthesis of advanced AOR/HER bifunctional catalysts sheds light on new robust AOR catalysts for electro-oxidation of ammonia and moves toward practical applications.

2. Results and Discussion

2.1. Structure and Morphology

Two oxides with K_2NiF_4 structure, $\text{La}_{0.5}\text{Sr}_{1.5}\text{NiO}_{4-\delta}$ (LSN) and 10% Cu doped LSN ($\text{La}_{0.5}\text{Sr}_{1.5}\text{Ni}_{0.9}\text{Cu}_{0.1}\text{O}_{4-\delta}$, LSNC), were synthesized by a modified Pechini method. Figure 1b demonstrates the XRD patterns of these two prepared samples. Both samples were single-phase and conformed with the body-centered tetragonal structure of $\text{La}_{0.5}\text{Sr}_{1.5}\text{NiO}_{3.938}$, sharing a space group of $I4/mmm$ (ICDD: 04-023-3096). When increasing the amount of Cu to 0.2, the product ($\text{La}_{0.5}\text{Sr}_{1.5}\text{Ni}_{0.8}\text{Cu}_{0.2}\text{O}_{4-\delta}$) is no longer a pure phase (Figure S1, Supporting Information) due to the segregation of Sr. Instead, it is a mixture of doped LaNiO_4 , NiO , SrCO_3 , and $\text{Sr}(\text{OH})_2 \cdot \text{H}_2\text{O}$. The phenomenon of Sr segregation at the surface is often observed in perovskite oxides and generally unfavorable for various catalytic processes.^[12–13] In the following experiment, we therefore focus on a low Cu doping level in LSN samples to avoid the formation of such secondary phases. As oxygen vacancies are beneficial to AOR, the two samples were annealed in Ar at 400 °C for 1 h. No additional peaks were observed in the annealed samples (namely: LSN-Ar and LSNC-Ar respectively) (Figure 1b).

SEM images showed typical morphologies of LSN, LSNC, LSN-Ar, and LSNC-Ar (Figure 1c; Figure S2, Supporting

Information). It is found that these four RP-type oxides have similar morphology. The average particle sizes were ≈ 200 nm and hardly changed with the doping or annealing process. TEM results confirm the morphology structure (Figure 1d). Figure 1e shows a HRTEM image of the LSNC-Ar. The clear crystal fringes with lattice spacing of 0.23 nm belong to (112) plane of LSNC-Ar sample. The HAAD-STEM and corresponding EDS elemental mappings in Figure 1f suggests uniform distribution of the La, Sr, Ni, Cu, and O elements.

2.2. Bifunctional Catalytic Activities

The AOR activities of these four oxide catalysts were measured in an alkaline solution. CV and LSV curves of the LSN catalyst are shown in Figure S3 (Supporting Information). This sample showed a pair of similar redox peaks in 0.5 M KOH media, which attribute to the transformation between the Ni^{2+} and Ni^{3+} species.^[7b,23] When 55×10^{-3} M NH_4Cl was added into the electrolyte, no evident change in current density or peak position was observed, indicating that the LSN sample is not active toward AOR. The same phenomenon was also found in the LSN-Ar sample, shown in Figure 2a. When Cu was introduced into B-site of LSN, the CV and LSV curves of LSNC in 0.5 M KOH and 0.5 M KOH + 55×10^{-3} M NH_4Cl (Figure S4, Supporting Information) showed different behavior. A higher current density could be observed when ammonia was added into the electrolyte, though the current density was still not high enough. However, a remarkable increase in anodic current density was observed in the LSNC-Ar sample when NH_4Cl was added (Figure 2a). The current density of LSNC-Ar located at 0.53 V versus Ag/AgCl is ≈ 13.4 mA cm^{-1} , which is around double that of the perovskite-based AOR catalyst previously studied.^[6d] To gain further insight into the effects of Cu and oxygen vacancies on ammonia oxidation performances, the LSV curves of LSN-Ar, LSNC, and LSNC-Ar were studied and shown in Figure 2b and Figure S4 (Supporting Information). The results prove that only when Ni and Cu coexist at the B site, the oxides show good AOR activity, indicating the synergistic interplay of Ni and Cu that is in agreement with our previous studies.^[6d,7b,24] Furthermore, the AOR activity could be significantly improved when introducing more oxygen vacancies into the lattice. This high current density is beneficial in speeding up the ammonia decomposition process, thereby improving the ammonia removal efficiency of the ammonia electrolyzer. For comparison, Figure 2c presents typical CV curves for the PtIr/C catalyst in 0.5 M KOH in the presence and absence of 55×10^{-3} M NH_4Cl , showing an ammonia oxidation peak in the potential range of -0.4 to -0.1 V versus Ag/AgCl, which is consistent with the results from a previous report.^[25] A small pre-peak at ≈ -0.7 V is likely attributed to the chemical adsorption of ammonia.^[25–26] Although PtIr/C has a lower oxidation potential to LSNC-Ar, the low current density of precious metal restricts its application at low voltage in ammonia electrolysis. Considering the price and electrochemical activity of oxide electrocatalysts, LSNC-Ar is still a good candidate to AOR catalyst. Moreover, the experimental current density versus the scan rate in LSNC-Ar is displayed in Figure S5a (Supporting Information). The CV curves exhibited a distinct linear trend against

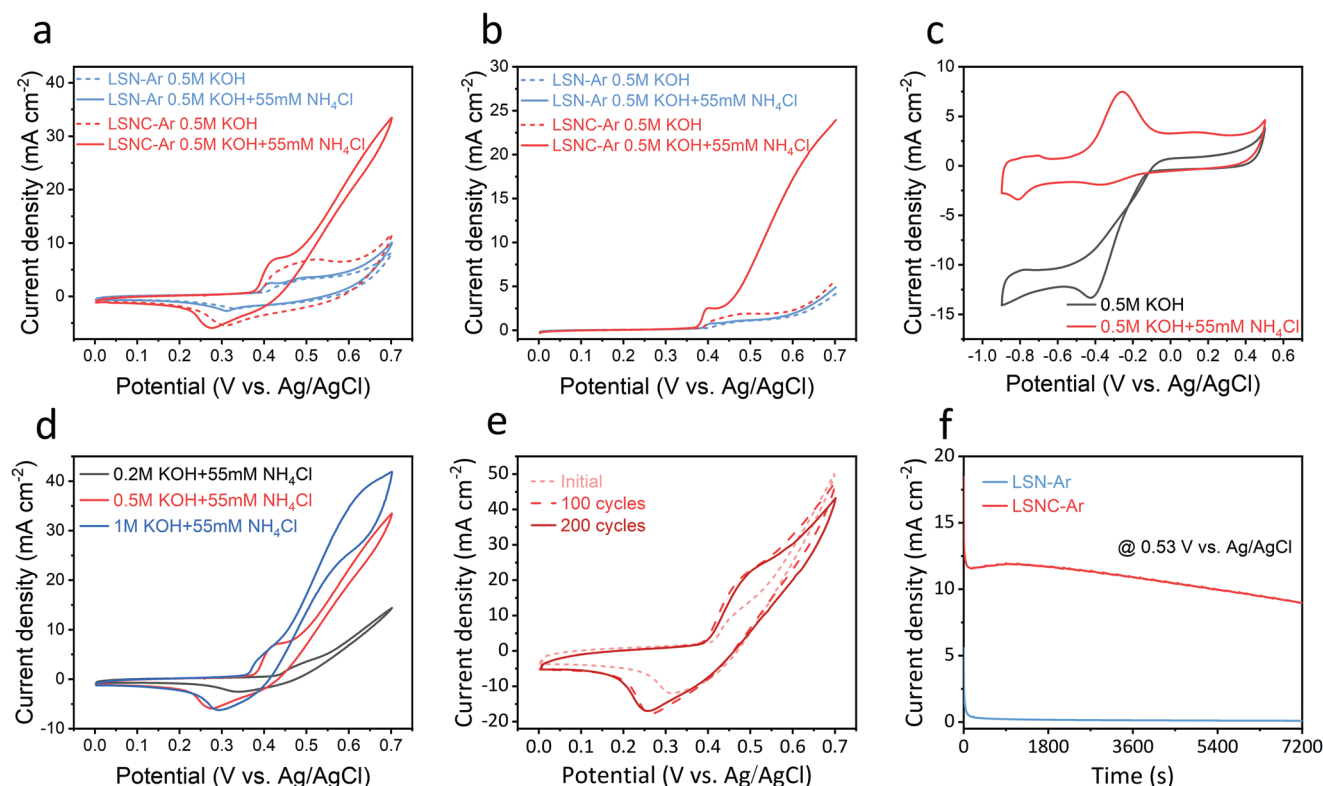


Figure 2. AOR activity. a) CV and b) LSV curves of LSN-Ar and LSNC-Ar in 0.5 M KOH, 0.5 M KOH + 55×10^{-3} M NH_4Cl . c) CV curves of PtIr/C in 0.5 M KOH, 0.5 M KOH + 55×10^{-3} M NH_4Cl . d) CV curves of LSNC-Ar in 0.2 M/0.5 M/1 M KOH + 55×10^{-3} M NH_4Cl . e) CV curves of LSNC-Ar initially, after 100 cycles and after 200 cycles in 0.5 M KOH with 55×10^{-3} M NH_4Cl at a scan rate of 50 mV s^{-1} . f) Chronoamperogram of LSN-Ar and LSNC-Ar electrodes in 0.5 M KOH with 55×10^{-3} M NH_4Cl at fixed potential of 0.53 V versus Ag/AgCl.

scan rates ($2\text{--}50 \text{ mV s}^{-1}$). From the corresponding calibration plot, a linear relationship ($R^2 = 0.998$) between the square root of the scan rates and the values of current density are observed, strongly suggesting that the AOR process was influenced by mass transfer limitations.^[27]

The ammonia oxidation activity is crucially determined by conditions such as alkalinity and ammonia concentration. Figure 2d illustrates the influence of pH on AOR activity, revealing that a higher alkaline concentration resulted in a larger current density. The AOR activity of LSNC-Ar was poor when 0.2 M KOH was added into the ammonia solution. At a potential of 0.53 V versus Ag/AgCl, the current density rose from 13.4 to 22.9 mA cm^{-2} as the OH^- concentration increased from 0.5 to 1 M. The favourable effect of alkaline environment was further verified by the LSV curves in Figure S6 (Supporting Information). The charge transfer resistance was considerably reduced in highly alkaline solution, showing fast mass transfer and charge transport at increasing concentrations of KOH (Figure S7, Supporting Information). The effect of ammonia content was also confirmed by CV and LSV curves, highlighted in Figure S8 (Supporting Information). The current density rose from 7.2 to 13.5 mA cm^{-2} when the ammonia concentration was increased from 20 to $100 \times 10^{-3} \text{ M}$ at a potential of 0.53 V versus Ag/AgCl. These findings show that increasing the pH value and ammonia concentration improves AOR activity.

Long-term stability is another essential criterion for the application of catalysts. The CV curves of LSNC-Ar electrode

in 0.5 M KOH + $55 \times 10^{-3} \text{ M}$ NH_4Cl solution were measured over 200 cycles at a scan rate of 50 mV s^{-1} (Figure 2e). An obvious increase in current density at 0.5 V versus Ag/AgCl was observed after the first 100 cycles, which was attributed to the activation of catalyst possibly due to the formation of metal hydroxides or oxyhydroxides.^[7b,23] Then, the current density slightly decreased after 100 cycles due to the consumption of ammonia. Chronoamperogram testing was further studied to evaluate the stability of the perovskite electrode with an anodic potential fixed at 0.53 V versus Ag/AgCl in 0.5 M KOH + $55 \times 10^{-3} \text{ M}$ NH_4Cl (Figure 2f). Compared to the low activity of LSN-Ar, the LSNC-Ar catalyst was able to hold excellent AOR activity based on its high current density. It is worth noting that the current density of LSNC-Ar gradually increased during the first 1000 s and then decreased, which is consistent with the observation seen by CV testing. All of the above results demonstrate that the LSNC-Ar catalyst exhibits excellent stability toward AOR.

Highly active bifunctional materials for AOR and HER have never been more in demand for the development of ammonia electrolysis technology; thus, it is highly desirable to develop bifunctional materials that can deliver considerable catalytic activities with good stability under alkaline conditions. RP oxides have been reported to be good HER catalysts.^[28] To explore the possibility of the LSNC-Ar as a bifunctional material for ammonia electrolysis, HER activity of the LSNC-Ar catalyst was evaluated via CV, LSV, and chronoamperometry in

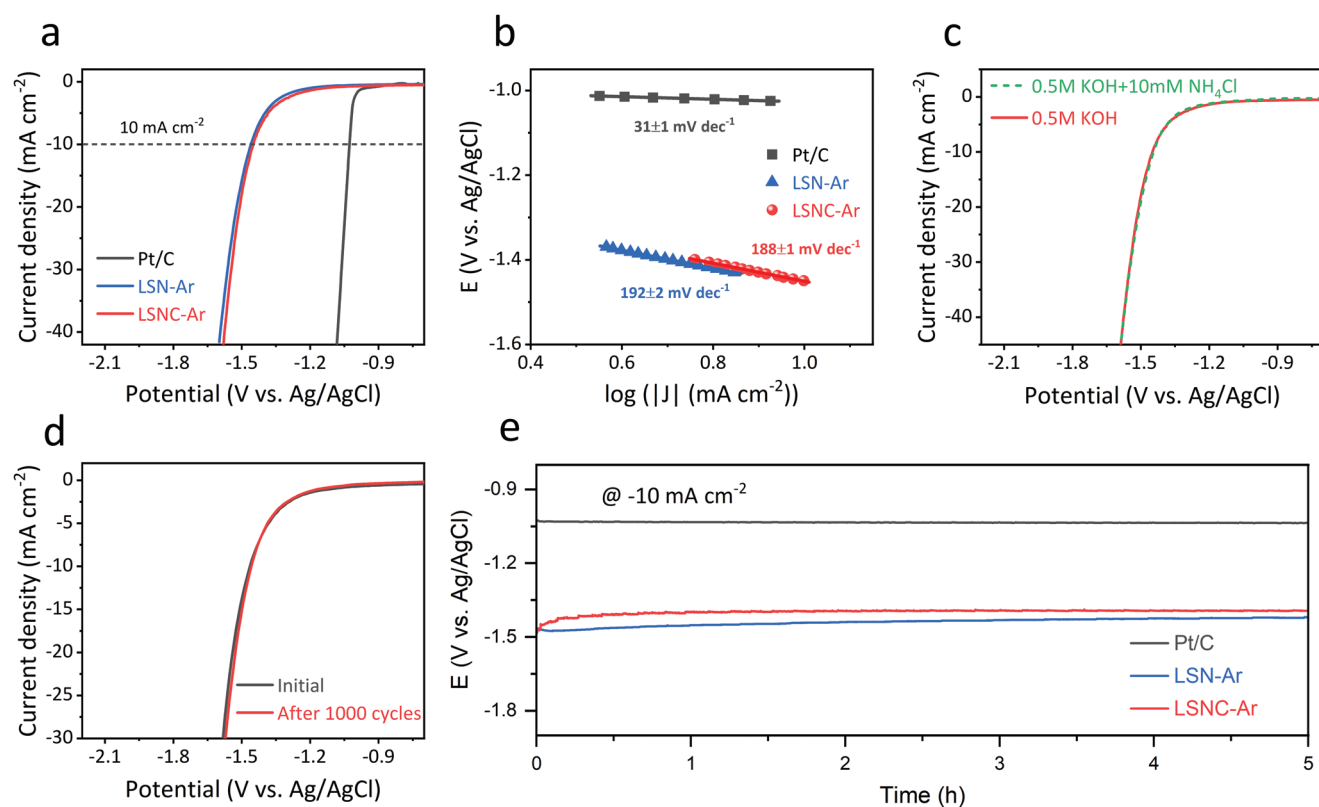


Figure 3. HER activity. a) HER polarization curves and b) Tafel plots of LSN-Ar, LSN-C-Ar and Pt/C catalysts in Ar-saturated 0.5 m KOH solution. c) HER polarization curves of LSN-C-Ar catalyst in Ar-saturated 0.5 m KOH and 0.5 m KOH + 10×10^{-3} m NH_4Cl solution. d) Polarization curves of LNC055-Ar initially and after 1000 cycles in 0.5 m KOH. e) Chronopotentiometry curves of LSN-Ar, LSN-C-Ar, and Pt/C catalysts in 0.5 m KOH at fixed potential of -10 mA cm^{-2} .

0.5 m KOH solution at room temperature. For comparison, the as-prepared LSN-Ar and commercial Pt/C catalysts were also tested under the same test conditions (Figure 3a). The Pt/C electrode had remarkable HER activity in alkaline conditions, which is consistent with prior studies.^[29] Both LSN-Ar and LSN-C-Ar can effectively catalyze HER with a potential as low as ≈ -1.15 V versus Ag/AgCl (defined here as the potential at which HER current density is -1.0 mA cm^{-2}). The potential required to deliver the current density of -10 and -20 mA cm^{-2} for these two perovskite catalysts are -1.46 and -1.45 V versus Ag/AgCl respectively. The Tafel slopes for LSN-Ar and LSN-C-Ar are also close in value, indicating that the introduction of Cu has negligible effect on HER activity. Although the HER performance of LSN-C-Ar is not as high in comparison to the best HER catalyst to date, this only plays a small effect on the overall ammonia electrolysis process since the performance is largely dependent on ammonia oxidation.^[30]

HER activity in the presence of ammonia is a challenging issue for HER catalysts. In contrast to common noble-metal catalysts where HER activity is significantly reduced due to the weaker metal-hydrogen underpotential deposition bonds, Ni-based catalysts maintain good HER activity in the presence of ammonia solution.^[31] This is also found in LSN-C-Ar catalyst. The polarization curve of the oxide catalyst showed negligible change in the presence of NH_4Cl , indicating that ammonia does not significantly alter the HER activity (Figure 3c). Durability

tests by continuous cycling in the range of -0.6 to -1.6 V were conducted. As shown in Figure 3d, after 1000 cycles, LSN-C-Ar showed a slight decline, indicating good stability for HER in alkaline media. The long-term stability of LSN-C-Ar was further confirmed by chronopotentiometry tests at a current density of -10 mA cm^{-2} , while the Pt/C catalyst showed superior stability as expected (Figure 3e). In view of the activity, durability and cost, LSN-C-Ar is an excellent AOR and HER bifunctional catalyst, making it an ideal material for ammonia electrolysis.

2.3. Symmetric Ammonia Electrolyzer Performance

A symmetric ammonia electrolyzer based on LSN-C-Ar as both the anode and cathode (SAE-LSN-C-Ar) was assembled, as shown in Figure 4a. Since the ammonia concentration in the real wastewater sample was found to be ≈ 2000 ppm, the performance of the SAE was first tested with a synthesized ammonia solution possessing a similar concentration. An ammonia solution with a relatively low concentration of 2177 ppm was prepared and confirmed by the spectrophotometer and then added 0.5 m KOH. The polarization curve of the SAE-LSN-C-Ar was performed with a sweep rate of 1 mV s^{-1} (Figure 4b). In order to be consistent with previous work and avoid the effects of water splitting, the applied cell voltage was fixed at 1.22 V .^[6d] In order to rule out the influence of the carbon cloth substrate,

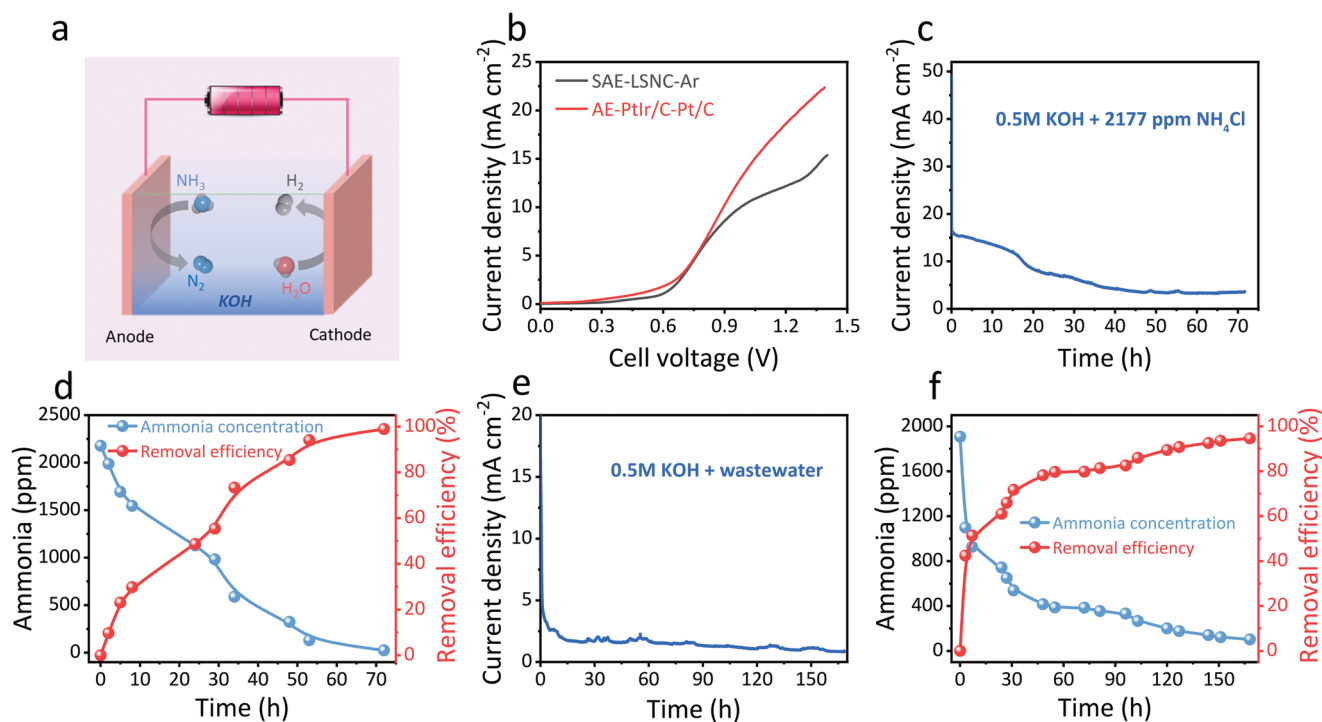


Figure 4. Performances. a) The schematic diagram of symmetric electrolyzer. b) LSVs data of SAE-LSNC-Ar and AE-PtIr/C-Pt/C in 0.5 m KOH + 2177 ppm NH_4Cl with a sweep rate of 1 mV s^{-1} . c) Record of electrolysis current density, d) the concentration profile of ammonia and removal efficiency of SAE-LSNC-Ar in the 0.5 m KOH + 2177 ppm NH_4Cl . e) Record of electrolysis current density, f) the concentration profile of ammonia and removal efficiency in SAE-LSNC-Ar in real wastewater + 0.5 m KOH.

the performance of symmetric ammonia electrolyzer based on carbon cloth (SAE-carbon cloth) was also measured. From Figure S9 (Supporting Information) it can be seen the the current density of the cell was very low and almost no ammonia was decomposed under a cell voltage of 1.22 V. As we know, the best known AOR and HER catalysts is PtIr/C and Pt/C respectively, so an AE based on PtIr/C anode and Pt/C cathode (AE-PtIr/C-Pt/C) was conducted under similar conditions for comparison. The performance of AE-PtIr/C-Pt/C is slight higher than that of SAE-LSNC-Ar below the cell voltage of 0.8 V (Figure 4b), due to the lower oxidation potential of PtIr/C catalyst (Figure 2a, c). Although the current density of the precious metal-based SA rose faster at an applied voltage above 0.8 V, the high current density of SAE-LSNC-Ar at high applied voltage indicates excellent activity and benefits from the use of low costing materials.

The electrolysis of ammonia solution in SAE-LSNC-Ar was examined and the current density of the cell was recorded in Figure 4c. In a 72-h test, the current density was high in the first 20 h and then decreased against electrolysis time due to the consumption of ammonia in the electrolyte. The ammonia concentration gradually decreased over time and the removal efficiency increased to about 100% after operating for 72 h (Figure 4d). This result indicates SAE-LSNC-Ar is a powerful electrochemical device for the complete removal of ammonia, making it a candidate for wide applications in ammonia-containing wastewater treatment.

The performance of the SAE-LSNC-Ar in real wastewater was then investigated using wastewater collected from the

Lochhead Landfill Site in Scotland.^[4b,6d] When wastewater + 0.5 m KOH was used as the electrolyte, the current density was initially high, at $\approx 5.0 \text{ mA cm}^{-2}$ (Figure 4e). After an operating period of 170 h, the current density dropped below 0.8 mA cm^{-2} . The concentration of ammonia decreased from 1908 to 102 ppm, and the ammonia removal efficiency reached $\approx 95\%$ (Figure 4f). This performance is better than most ammonia removal efficiencies in practical wastewater by traditional or modern methods, such as electrolysis, microbial electrolysis or photocatalysis.^[32] In addition, the assembled SAE-LSNC-Ar showed the highest efficiency among electrochemical removal of ammonia in landfill leachate (Table 1). It is worth noting that the ammonia removal efficiency of SAE-LSNC-Ar, 95% is also much higher than the 70% achieved when perovskite oxide $\text{LaNi}_{0.5}\text{Cu}_{0.5}\text{O}_{3-\delta}\text{-Ar}$ was used as the AOR catalyst in our previous study which also utilised the same real wastewater batch.^[6d]

2.4. Mechanism

It is widely understood that oxygen vacancies have a significant impact on the electronic structure and surface chemistry of perovskites, resulting in improved catalytic activity.^[6d,11,12] Compared to single LaNiO_3 perovskite, the A-site of La in La_2NiO_4 RP oxide could be easily occupied by high content and low-valence Sr.^[13a,20] This substitution in the unique RP crystal structure not only leads to high concentration oxygen defects, but also maintains structural stability.^[18b] In our study, more

Table 1. Comparison of ammonia removal efficiency with literature results for ammonia electrolyzer.

Anode	Cathode	Wastewater	The initial Concentration of ammonia	Removal efficiency	Ref.
RuO ₂ /Ti	Stainless steel	Municipal wastewater	29.9 mg N/L	85% ammonia	[33]
CoZnO/graphite	Graphite	Aquaculture wastewater	3.69 ± 0.72 mg L ⁻¹ NH ₄ ⁺	>90% ammonia nitrogen	[34]
Pt/N-rGO	Mo ₂ C/N-rGO	Landfill leachate	2260 mg L ⁻¹ ammonia	70.7% NH ₄ ⁺ -N	[32g]
NiO-TiO ₂	Pd	Real wastewater	60 ± 2 mg-N L ⁻¹ ammonia	93% ammonia	[35]
RuO ₂ /Ti	Stainless steel	Rinse wastewater	2156 ± 50 mg L ⁻¹ ammonia	70% ammonia	[36]
Magnesium plate	Stainless steel mesh plate	Swine wastewater	426 ± 21 mg L ⁻¹ ammonia nitrogen	>90% ammonia nitrogen	[37]
TiRuSnO ₂	Stainless steel	Landfill leachate	366 mg dm ⁻³ NH ₄ ⁺ -N	65% ammonia	[38]
Ti/IrO ₂	Stainless steel	Municipal wastewater	≈24 mg L ⁻¹ ammonia	95% ammonia	[39]
LaNi _{0.5} Cu _{0.5} O _{3-δ} Ar	LaNi _{0.5} Cu _{0.5} O _{3-δ} Ar	Landfill leachate	2210 ppm ammonia	>70% ammonia	[6d]
LSNC-Ar	LSNC-Ar	Landfill leachate	2177 ppm ammonia	95% ammonia	This work

oxygen vacancies may be formed in the crystalline lattice as the partial doped Cu into B-sites and the subsequent annealing process. In order to determine the existence of oxygen vacancies directly, the oxygen stoichiometry of LSN-Ar and LSNC-Ar samples were measured by iodometric titration. The results show that the oxygen defect concentration in LSNC-Ar (15.21%) is very high and greater than that of LSN-Ar (13.13%). Combined with the electrochemical results (Figure 2; Figures S3 and S4, Supporting Information), it is evident that a high concentration of oxygen vacancies in LSNC-Ar have a vital effect on AOR catalytic performance.

The high electrical conductivity of RP oxides is another advantage that makes them suitable for electrolysis since fast charge transfer is favorable for electrochemical processes.^[14b] In general, RP oxides have mixed oxide-ionic and electronic conductivities, with the oxide ionic conduction originating from oxygen vacancies and the electronic conduction originating mostly from the BO₆ octahedra.^[40] In order to study the electronic conduction of the LSNC-Ar sample, LSN-Ar and LSNC-Ar bulks were tested through a four-probe method from room temperature to 90 °C to observe DC conductivity. From Figure 5a, both oxides exhibit semiconductor-like behavior within the temperature range. This phenomenon is similar to other reported RP structure oxides.^[41] In addition, the electrical conductivity of LSNC-Ar is higher than that of LSN-Ar due to the introduction of Cu into RP structure.^[42] The high electrical conductivity is key to minimize conduction losses, accelerating electron transfer, increasing the reaction area, and improving catalytic reactions in electrolysis.^[12] The Arrhenius plots of LSN-Ar and LSNC-Ar were shown in Figure S10 (Supporting Information) and the activation energy of LSNC-Ar (0.059(2) eV) is higher than that of LSN-Ar (0.066(1) eV). These values are consistent with that of other RP semiconductor oxide.^[43] It should be noted that, with similar composition, the conductivity of oxides with the K₂NiF₄ structure is lower than those with perovskite structure because the rock-salt layer in K₂NiF₄ structure is generally not an insulator for electronic conduction. However, a high-level Sr doping in La₂NiO₄ may result in higher electronic conductivity.

The synergistic effect between Ni and Cu in AOR catalyst has been demonstrated in previous reports. Bare Ni or Cu is almost inactive toward AOR as the metals bind to the N site of

ammonia either too weakly or too strongly.^[24] The inappropriate bond strength cannot efficiently accommodate the subsequent dehydrogenation reactions.^[8a] However, when Ni incorporated with Cu to form bimetal, the ammonia oxidation activity and stability of NiCu bimetal are excellent due to the synergistic effect between Ni and Cu. The positive effect of combining these elements together is also confirmed in the perovskite catalyst.^[6d] In the present work, Cu-undoped samples, e.g. LSN and LSN-Ar, are inactive toward AOR (Figure 2a; Figure S3, Supporting Information). As expected, when Cu is introduced into LSN, LSNC showed a higher current density in ammonia solution (Figure S4, Supporting Information). In addition, the best AOR activity was observed with the LSNC-Ar catalyst (Figure 2a,b), indicating the positive effect of synergistic effect and oxygen vacancy.

XRD analysis was conducted to check the material composition of LSNC-Ar electrodes before and after electrolysis, and is presented in Figure 5b. Before the electrolysis experiment, the LSNC-Ar electrode only consisted of the perovskite and carbon cloth substrate. After the electrolysis test, three new phases of KOH, NiCu(OH)₂, and SrCO₃ appeared on both anode and cathode electrodes. In RP oxides, it is generally recognized that oxygen vacancies are responsible for phase reconstruction and the exsolved phases tend to favor the reactions.^[44] In addition, Ni-based AOR catalysts always tend to transform to metal hydroxide or oxyhydroxide during the ammonia oxidation process where these materials are the true active sites for AOR.^[7b,24,35,45] In order to maintain electrical neutrality of the oxides, some A-site cations separated from the lattice and formed SrCO₃ in the LSNC-Ar anode after the electrolysis test (marked by LSNC-Ar anode). At the cathode side, it is worth noting that the diffraction peak intensity of RP oxide is greatly weakened, suggesting an abundant amount of oxides were converted to other crystalline and amorphous components during the HER process. Though the diffraction intensity of the new SrCO₃ phase is very high in the LSNC-Ar cathode after electrolysis (marked by LSNC-Ar cathode), there is little crystalline metal hydroxide. This indicates that some B-site cations may separate from the RP lattice and evolve into amorphous components. Experimental studies and calculations revealed that amorphous Ni(OH)₂ is a good HER catalyst, and it is more energetically favored for the hydrogen evolution in comparison

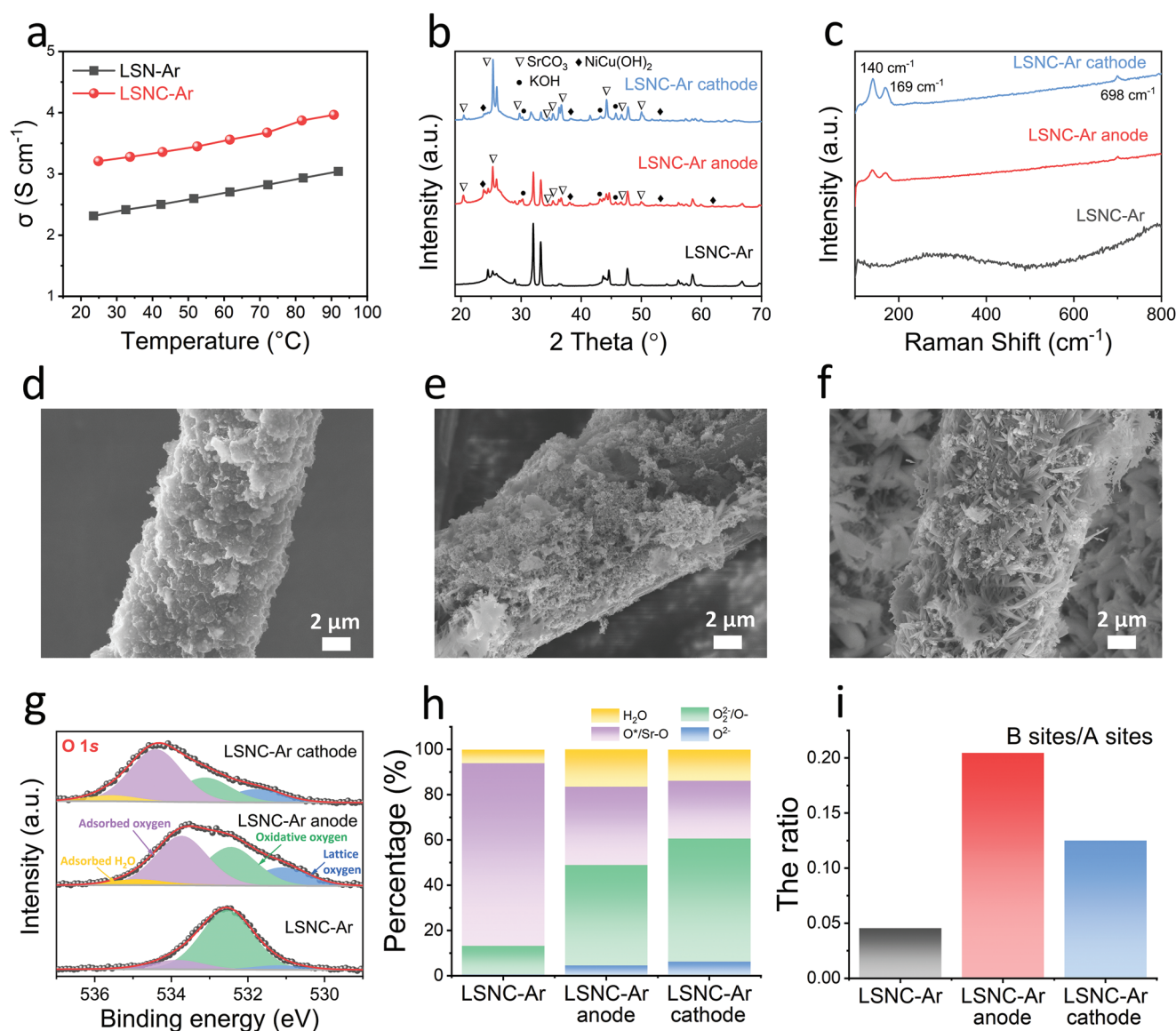


Figure 5. Mechanism. a) The DC conductivity of LSN-Ar and LSNC-Ar. b) XRD patterns and c) Raman spectra of LSN-Ar, LSNC-Ar anode, and LSNC-Ar cathode. SEM images of d) LSN-Ar electrode before test, e) LSNC-Ar anode and f) LSNC-Ar cathode after electrolysis test. g) XPS spectra of O 1s, h) the percentage of oxygen species and i) the ratio of B-site/A-site in LSN-Ar, LSNC-Ar, anode and LSNC-Ar cathode.

to its crystalline counterpart.^[46] Moreover, the heterostructure synergetic effects between amorphous $\text{Ni}(\text{OH})_2$ and the host may contribute to better HER activity.^[47] It is anticipated that crystalline and amorphous metal hydroxide may coexist on the surface. The structural evolution was also confirmed by Raman spectra. As shown in Figure 5c, the Raman peaks of SrCO_3 were observed in the LSNC-Ar anode and cathode electrodes, located at 140, 169, and 698 cm^{-1} .^[48] Combining the above results and assumptions, it is clear that the structural evolution during catalytic reactions promotes both AOR and HER activities.

To gain more insight into the structural changes, SEM images of LSN-Ar electrodes before and after electrolysis are exhibited in Figure 5d–f. LSN-Ar nanoparticles before the test were uniformly deposited on the carbon cloth, although some agglomerations of the particles were observed (Figure 5d).

According to EDS mapping images and EDS spectra (Figure S11, Supporting Information), elements of La, Sr, Ni, Cu, and O can be observed clearly. At the anode side, the LSNC-Ar particles were split into smaller nanoparticles. This phenomenon of size reduction after catalytic reaction is also observed in other papers and it can be attributed to the surface reconstruction and electrostatic driving force at the surface.^[6d,49] More active sites are created by reducing particle size, which are beneficial for ionic and electronic transportation and electrochemical processes in electrolysis. Besides the nanoparticles, a small number of nanorods were formed on the surface of carbon cloth, which were attributed to the new SrCO_3 phase (Figure 5e).^[50] The EDS analysis confirms that this electrode was still composed of La, Sr, Ni, Cu, and O (Figure S12, Supporting Information). At the cathode side, substantial nanorods were found after hydrogen

evolution and the SrCO_3 nanorods could be confirmed in the EDS mapping (Figure 5f; Figure S13, Supporting Information).

In addition, XPS measurements were conducted to analyze the surface of the LNSC-Ar catalyst before and after testing. XPS spectra of La 4d are fitted adapted from the La_2O_3 model (Figure S14, Supporting Information), and these samples only contained La^{3+} .^[51] The dominant doublet of Sr 3d, shown in green and purple (Figure S15, Supporting Information), are thought to be due to Sr bound to a halide, most likely SrF_2 , while the smaller doublet, depicted in orange and blue, are thought to be from SrO .^[52] Thus, all of the Sr is in the Sr^{2+} oxidation state. Figure 5g shows the O 1s XPS spectra of the LNSC-Ar, LSNC-Ar anode and cathode, which were deconvoluted into four characteristic subpeaks, including adsorbed H_2O at ≈ 534.9 eV, adsorbed oxygen or strontium-carbon bond at ≈ 533.7 eV ($\text{O}^*/\text{Sr}-\text{O}$), highly oxidative oxygen at ≈ 532.4 eV ($\text{O}_2^{2-}/\text{O}^-$), and lattice oxygen at ≈ 531.9 eV (O^{2-}).^[53] Based on the relative integrated area intensities of these fitted subpeaks, the percentages of the various oxygen species were plotted in Figure 5h. It has been demonstrated that $\text{O}_2^{2-}/\text{O}^-$ at the surface of materials correlates to the oxygen vacancy content and leads to a high oxygen ionic diffusion rate and electrical conductivity.^[53–54] The LSNC-Ar electrode before testing displays a high percentage of the highly oxidative species (80.7%), indicating the substantial amount of highly active surface oxygen vacancies. After electrolysis, the content of adsorbed oxygen and strontium-carbon bond at the anode and cathode sides increased from 12.6% to 44.4% and 54.4% respectively. These results support the high oxygen vacancy in the LSNC electrode and the formation of SrCO_3 after electrolysis.

The active site in K_2NiF_4 -type oxides is generally the B-site cations and increasing the number of active sites can improve catalytic reaction. In order to figure out the active sites before and after electrolysis, the ratios of B-site/A-site were calculated and compared in Figure 5i. In the original LSNC-Ar electrode, the ratio was very low and a great amount of A-site cations gathered at the surface. However, after the electrolysis test, the ratio of B-site/A-site increased significantly at both the anode and cathode sides, suggesting more B-sites were evolved and the phenomenon of Sr segregation relieved to some extent after AOR and HER. More active sites were exposed at the surface, resulting in good stability for long-term testing (Figure 2e,f and Figure 3d,e). Understanding the origins of the enhanced bifunctional ammonia electrolysis for the K_2NiF_4 -type LNSC-Ar versus the simple perovskite catalyst provides critical guidance in designing better materials. All the factors described above, namely, the enhanced electrical conductivity, oxygen vacancy-enriched oxide, and the structural evolution during catalytic process, support LSNC-Ar to be an outstanding candidate material for both AOR and HER.

3. Conclusions

In summary, a monolayer RP-type oxide, $\text{La}_{0.5}\text{Sr}_{1.5}\text{Ni}_{0.9}\text{Cu}_{0.1}\text{O}_{4-\delta}\text{Ar}$ (LSNC-Ar), was prepared via a modified Pechini method and subsequently annealed in Ar. LSNC-Ar can act as a robust AOR anode and achieve 13.4 mA cm^{-1} at potential of 0.53 V versus Ag/AgCl in 0.5 KOH with $55 \times 10^{-3} \text{ M}$ NH_4Cl . The

kinetics of AOR is strongly dependent on the alkaline concentration and ammonia concentration, which showed higher pH and ammonia content can improve the AOR activity of LSNC-Ar catalyst. In addition, this RP oxide also showed HER catalytic activity. When constructing an SAE using this bifunctional catalyst, the performance of our SAE-LSNC-Ar showed only slight difference to that of AE-PtIr/C-Pt/C below the cell voltage of 0.8 V. Although the current density of precious metal-based SA rose faster above 0.8 V, the high current density of SAE-LSNC-Ar indicates excellent activity with lower costing materials. As a result, the system is capable of 95% ammonia removal at a cell voltage as low as 1.22 V in a real landfill leachate. The excellent bifunctional activities of LSNC-Ar can be considered to mainly originate from the following factors: 1) the enhanced electrical conductivity due to heavy Sr doping; 2) oxygen vacancy-enriched oxide due to firing in Ar; 3) the synergistic interplay of Ni and Cu. To the best of our knowledge, this is the first report on using oxides with a K_2NiF_4 structure as an AOR catalyst and for the purpose of ammonia electrolysis. The strategy in this work demonstrates great potential toward designing highly active and stable bifunctional catalysts for various electrochemical devices including symmetric ammonia electrolyzers.

4. Experimental Section

Chemicals: The chemicals used in this experiment are lanthanum(III) nitrate hexahydrate ($\text{La}(\text{NO}_3)_3 \cdot 6\text{H}_2\text{O}$, 99.9%, Alfa Aesar), strontium nitrate ($\text{Sr}(\text{NO}_3)_2$, 98%, Alfa Aesar), nickel(II) nitrate hexahydrate ($\text{Ni}(\text{NO}_3)_2 \cdot 6\text{H}_2\text{O}$, 99.8%, Alfa Aesar), copper(II) nitrate 2.5-hydrate ($\text{Cu}(\text{NO}_3)_2 \cdot 2.5\text{H}_2\text{O}$, 99.8%, Alfa Aesar), citric acid (CA, 99+%, Alfa Aesar), ethylene diamine tetraacetic acid (EDTA, 99%, Alfa Aesar), ammonia solution ($\text{NH}_3 \cdot \text{H}_2\text{O}$, 35%, 0.88 g/mL, Fisher Chemical), ammonium chloride (NH_4Cl , 99.5%, Alfa Aesar), potassium hydroxide (KOH, 85%, Alfa Aesar), isopropanol ($\text{C}_3\text{H}_8\text{O}$, $\geq 99.8\%$, Sigma-Aldrich), carbon black (Cabot Vulcan XC-72R), and Nafion solution (5% in lower aliphatic alcohols and water, Sigma-Aldrich). All reagents were directly used without further refinement. The deionized water was supplied for the entire experiment.

Materials Synthesis: $\text{La}_{0.5}\text{Sr}_{1.5}\text{Ni}_{1-x}\text{Cu}_x\text{O}_{4-\delta}$ samples ($x = 0, 0.1$; denoted as LSN-Ar, LSNC-Ar respectively) were synthesized by a modified Pechini method and subsequently annealed in Ar.^[13a] In a synthesis typical procedure, 0.015 mol $\text{La}(\text{NO}_3)_3 \cdot 6\text{H}_2\text{O}$, 0.045 mol $\text{Sr}(\text{NO}_3)_2$, 0.027 mol $\text{Ni}(\text{NO}_3)_2 \cdot 6\text{H}_2\text{O}$, and 0.003 mol $\text{Cu}(\text{NO}_3)_2 \cdot 2.5\text{H}_2\text{O}$ were dissolved in 200 mL deionized water. CA and EDTA were then added to the solution at a ratio of 1.2:1 and 1:1 with the total metal nitrate salts respectively. The mixture was neutralized with ammonia solution until the pH value reached 8 and a clear blue solution formed. Some white precipitate appeared during the process, then disappeared when the pH value increased to a value above 7.^[18b] The blue solution was continuously stirred at 90 °C overnight to yield a navy blue gel. The gel was then heated to 350 °C and held at this temperature for 2 h to form dried powders. The solid precursor was cooled to room temperature and ground by an agate mortar and pestle, then further calcined in a muffle furnace at 600 °C for 3 h. Subsequently, the cooled powder was ground again and heated at 1000 °C for 4 h in air. The as-prepared powder was labelled as LSNC. In order to obtain an oxygen vacancy-enriched LSNC-Ar catalyst, the LSNC powder was put into a tube furnace and annealed in Ar at 400 °C for 1 h. To obtain LSNC-Ar bulk, the LSNC powders were grounded and sieved through a 200-mesh screen to form a homogeneous fine product. For conductivity measurements, the LSNC powders prepared in air were pressed into pellets with diameter of 13 mm and a thickness of roughly 3 mm. Then, the pellet was fired in air at 1100 °C for 4 h and annealed in

Ar at 400 °C for 1 h. Silver paste was coated on both sides of the sintered powder before conductivity measurements.

Electrode Preparation: The catalyst inks for the AOR and HER were prepared according to literature.^[6d] As carbon fiber had proven to be a good substrate for ammonia electrolysis at low concentration,^[7a] carbon cloth (Fuel Cell Store, Product code: 7 302 007) was used as the conductive substrate throughout the experiment. Before electrode preparation, carbon clothes were washed sequentially in dilute hydrochloric acid, deionized water, and isopropanol. The catalyst ink was prepared by mixing 0.1 g catalyst, 0.02 g carbon black, 500 µL deionized water, 500 µL isopropanol, and 40 µL Nafion solution. The ink was continuously stirred overnight at room temperature. The slurry was then brushed over the carbon cloth and dried overnight at room temperature. For comparison, Pt/C (commercial 20 wt.% platinum on carbon black, Alfa Aesar) and PtIr/C electrodes (20 wt.% metal on carbon black, prepared by reduction process according to the literature^[55]) were prepared in the same way. For example, the Pt/C ink was prepared by mixing 0.1 g Pt/C, 500 µL deionized water, 500 µL isopropanol, and 40 µL Nafion solution. The loading of the oxide catalyst/C, Pt/C, and PtIr/C was 3.6, 3.5 and 3.0 mg cm⁻² respectively. When considering the active materials only, the loading of oxide, Pt, and PtIr was 3.0, 0.7 and 0.6 mg cm⁻² respectively.

Materials Characterizations: X-ray diffraction (XRD) was conducted on the Malvern Panalytical Empyrean. Scanning electron microscopy (SEM) images were collected through a field emission SEM (FE-SEM, Zeiss Supra 55-VP). High resolution transmission electron microscope (HRTEM), high-angle annular dark-field transmission electron microscope (HAAD-TEM) and energy-dispersive X-ray spectroscopy (EDS) mapping were performed to analyze the morphology and elemental composition by JEOL ARM 200F. Raman microscopy was performed with a 532 nm wavelength excitation (LabRAM HR800, HORIBA Jobin Yvon). X-ray photoelectron spectroscopy (XPS) measurements were conducted using a monochromated Al K_α X-ray source on a Kratos Axis Ultra DLD spectrometer (Kratos Analytical, Manchester, UK). Data were taken at a take-off angle of 90° with respect to the surface plane and analyzed using the Casa XPS package, using mixed Gaussian-Lorentzian lineshapes and Shirley backgrounds. In order to prevent the surfaces becoming positively charged during the test, charge neutralization was employed and the spectra subsequently referenced to the C—C/C—H peak at 285.0 eV during analysis.

Electrochemical Measurements: AOR and HER performance tests were both conducted at room temperature in a standard three-electrode system. The prepared electrode, Ag/AgCl (sat. KCl) electrode, and platinum foil were used as the working electrode, reference electrode, and counter electrode respectively.

For the AOR test, the electrochemical characterization was determined by cyclic voltammetry (CV), linear sweep voltammetry (LSV), and chronoamperometry using the Solartron 1287A Electrochemical Station. Electrochemical impedance spectroscopy (EIS) was tested using the Solartron 1260 Electrochemical Station. All oxide samples were electrochemically activated between 0 to 0.7 V versus Ag/AgCl (3 cycles) at a scan rate of 50 mV s⁻¹. Then, the CV and LSV measurements were recorded in an alkaline solution from potentials of 0 to 0.7 V versus Ag/AgCl at scan rates of 10 and 2 mV s⁻¹ respectively. The CV curves of PtIr/C catalyst were measured from -0.9 to 0.5 V versus Ag/AgCl at scan rates of 10 mV s⁻¹. Chronoamperograms of the LSN-Ar and LSNC-Ar electrodes were recorded in 0.5 M KOH with 55 × 10⁻³ M NH₄Cl at fixed potential of 0.53 V versus Ag/AgCl. EIS for AOR was carried out by applying a fixed potential of 10 mV bias at a frequency range of 1 MHz to 0.01 Hz.

For HER performance, the electrochemical characterization was conducted by the Solartron 1470E multichannel cell test system. Prior to HER tests, the solution was deaerated by continuous purging with high purity Ar for 30 min. Then, LSV curves for HER were measured between -0.6 and -1.6 V versus Ag/AgCl at a scan rate of 2 mV s⁻¹. CV curves were conducted at 10 mV s⁻¹ for 1000 cycles in 0.5 M KOH. Chronopotentiometry of LSN-Ar, LSNC-Ar, and Pt/C electrodes were carried out at a fixed potential of -10 mA cm⁻².

The electrical conductivities of the samples were measured in Ar by a pseudo four-probe DC method as described earlier.^[56] The measurements were recorded from room temperature to 100 °C at a rate of 0.2 °C min⁻¹. The bulk sample was placed onto an alumina support and four silver wires were fixed onto the sample using silver paste. A constant potential of 10 mV was applied by the Solartron 1470E multichannel cell test system.

Determination of Oxygen Vacancy Concentration by Iodometric Titrations: Iodometric titration was used to test the oxygen vacancy content of RP oxides.^[6d] First, 30 mg oxide was dissolved in dilute hydrochloric acid under Ar atmosphere. Subsequently, excess KI and five drops of starch indicator were added into the solution. Then mixed solution was titrated by 0.02 M Na₂S₂O₃ solution until it was clear and colorless.



According to equation 3, the product of I₂ will be reduced by Na₂S₂O₃. So, the molar amount of Ni³⁺ could be obtained and the oxygen vacancy concentration was calculated based on the amount of oxide and thiosulfate solution.

Symmetric Ammonia Electrolyzer Performance Evaluation: The LSNC-Ar electrodes were directly used as bifunctional catalysts without any pre-activation and further treatment. A solution containing 25 mL 0.5 M KOH + 2177 ppm NH₄Cl solution was used as the electrolyte. The concentration of ammonia was confirmed by a spectrophotometer (S-22 UV/vis, Boeco, Germany). The real wastewater was collected from Lochhead Landfill Site in Scotland. Twenty five milliliter of wastewater was filtered before use.

Supporting Information

Supporting Information is available from the Wiley Online Library or from the author.

Acknowledgements

This work was supported by the (Grant Nos. EP/G030995/1) and the Innovate UK (Grant Nos. 104010 and 133714). The authors thank Shields Jane at Living Water Ltd for providing the landfill leachate.

Conflict of Interest

The authors declare no conflict of interest.

Data Availability Statement

The data that support the findings of this study are available from the corresponding author upon reasonable request.

Keywords

ammonia removal, AOR/HER bifunctional catalysts, K₂NiF₄ structures, symmetric ammonia electrolyzers, wastewater

Received: April 29, 2022

Revised: June 15, 2022

Published online:

- [1] a) J. G. Chen, R. M. Crooks, L. C. Seefeldt, K. L. Bren, R. M. Bullock, M. Y. Darensbourg, P. L. Holland, B. Hoffman, M. J. Janik, A. K. Jones, M. G. Kanatzidis, P. King, K. M. Lancaster, S. V. Lyman, P. Pfomm, W. F. Schneider, R. R. Schrock, *Science* **2018**, 360, eaar6611; b) J. S. Cardoso, V. Silva, R. C. Rocha, M. J. Hall, M. Costa, D. Eusébio, *J. Clean Prod.* **2021**, 296, 126562; c) G. Jeerh, M. Zhang, S. Tao, *J. Mater. Chem. A* **2021**, 9, 727; d) R. Lan, J. T. S. Irvine, S. Tao, *Int. J. Hydrog. Energy* **2012**, 37, 1482.
- [2] D. R. MacFarlane, P. V. Cherepanov, J. Choi, B. H. R. Suryanto, R. Y. Hodgetts, J. M. Bakker, F. M. Ferrero Vallana, A. N. Simonov, *Joule* **2020**, 4, 1186.
- [3] V. P. Aneja, J. Blunden, K. James, W. H. Schlesinger, R. Knighton, W. Gilliam, G. Jennings, D. Niyogi, S. Cole, *J. Environ. Qual.* **2008**, 37, 515.
- [4] a) M. Li, C. J. Weschler, G. Beko, P. Wargocki, G. Lucic, J. Williams, *Environ. Sci. Technol.* **2020**, 54, 5419; b) M. Zhang, P. Zou, G. Jeerh, S. Chen, J. Shields, H. Wang, S. Tao, *ACS Sustainable Chem. Eng.* **2020**, 8, 12817.
- [5] a) J. Huang, N. R. Kankanamge, C. Chow, D. T. Welsh, T. Li, P. R. Teasdale, *J. Environ. Sci.* **2018**, 63, 174; b) G. Jeerh, P. Zou, M. Zhang, S. Chen, J. Humphreys, S. Tao, *Sep. Purif. Technol.* **2022**, 297, 121451.
- [6] a) G. Zhang, J. Ruan, T. Du, *ACS ES&T Eng.* **2020**, 1, 310; b) X. Xi, Y. Fan, K. Zhang, Y. Liu, F. Nie, H. Guan, J. Wu, *Chem. Eng. J.* **2022**, 435, 134818; c) N. Akagi, K. Hori, H. Sugime, S. Noda, N. Hanada, *J. Catal.* **2022**, 406, 222; d) M. Zhang, H. Li, X. Duan, P. Zou, G. Jeerh, B. Sun, S. Chen, J. Humphreys, M. Walker, K. Xie, S. Tao, *Adv. Sci.* **2021**, 8, 2101299; e) B. K. Boggs, G. G. Botte, *J. Power Sources* **2009**, 192, 573.
- [7] a) E. P. Bonnin, E. J. Biddinger, G. G. Botte, *J. Power Sources* **2008**, 182, 284; b) W. Xu, D. Du, R. Lan, J. Humphreys, D. N. Miller, M. Walker, Z. Wu, J. T. S. Irvine, S. Tao, *Appl. Catal. B-Environ.* **2018**, 237, 1101.
- [8] a) J. A. Herron, P. Ferrin, M. Mavrikakis, *J. Phys. Chem. C* **2015**, 119, 14692; b) N. J. Bunce, D. Bejan, *Electrochim. Acta* **2011**, 56, 8085; c) Y. Li, H. Wang, C. Priest, S. Li, P. Xu, G. Wu, *Adv. Mater.* **2021**, 33, 2000381; d) Q. Xue, Y. Zhao, J.-Y. Zhu, Y. Ding, T. Wang, H.-Y. Sun, F. Li, P. Chen, P. Jin, S. Yin, Y. Chen, *J. Mater. Chem. A* **2021**, 9, 8444; e) J. Liu, Z. Liu, H. Wang, B. Liu, N. Zhao, C. Zhong, W. Hu, *Adv. Funct. Mater.* **2021**, 32, 2110702.
- [9] L. Szpyrkowicz, S. N. Kaul, R. N. Neti, S. Satyanarayan, *Water Res.* **2005**, 39, 1601.
- [10] a) N. Hanada, Y. Kohase, K. Hori, H. Sugime, S. Noda, *Electrochim. Acta* **2020**, 341, 136027; b) H. Huang, D. Zhang, G. Guo, Y. Jiang, M. Wang, P. Zhang, J. Li, *Chem. Eng. J.* **2018**, 335, 665.
- [11] S. Zhang, Y. Zhao, L. Yan, H. Jiang, X. Yang, Y. Wang, H. Song, X. Zhao, *Int. J. Hydrog. Energy* **2021**, 46, 39208.
- [12] M. Zhang, G. Jeerh, P. Zou, R. Lan, M. Wang, H. Wang, S. Tao, *Mater. Today* **2021**, 49, 351.
- [13] a) R. P. Forslund, C. T. Alexander, A. M. Abakumov, K. P. Johnston, K. J. Stevenson, *ACS Catal.* **2019**, 9, 2664; b) Y. Takeda, T. Hashino, H. Miyamoto, F. Kanamaru, S. Kume, M. Koizumi, J. Inorg. Nucl. Chem. **1972**, 34, 1599.
- [14] a) A. G. Ricciardulli, S. Yang, J. H. Smet, M. Saliba, *Nat. Mater.* **2021**, 20, 1325; b) X. Xu, Y. Pan, Y. Zhong, R. Ran, Z. Shao, *Mater. Horizons* **2020**, 7, 2519; c) P. Li, W. Yang, C. Tian, W. Zhao, Z. Lü, Z. Xie, C.-A. Wang, *J. Adv. Ceram.* **2021**, 10, 328; d) J. Irvine, J. Rupp, G. Liu, X. Xu, S. M. Haile, X. Qian, A. Snyder, R. Freer, D. Ekren, S. Skinner, O. Celikbilek, S. Chen, S. Tao, T. H. Shin, R. O'Hayre, J. Huang, C. Duan, M. Papac, S. Li, A. Russel, V. Celorio, B. Hayden, H. Nolan, X. Huang, G. Wang, I. Metcalfe, D. Neagu, S. G. Martin, *J. Phys. Energy* **2021**, 3, 031502.
- [15] G. Nirala, D. Yadav, S. Upadhyay, *J. Adv. Ceram.* **2020**, 9, 129.
- [16] I. B. Sharma, D. Singh, *Bull. Mater. Sci.* **1998**, 21, 363.
- [17] F. S. Oliveira, P. M. Pimentel, R. M. P. B. Oliveira, D. M. A. Melo, M. A. F. Melo, *Mater. Lett.* **2010**, 64, 2700.
- [18] a) A. Aguadero, M. J. Escudero, M. Perez, J. A. Alonso, V. Pomjakushin, L. Daza, *Dalton Trans.* **2006**, 36, 4377; b) A. Niemczyk, R. Merkle, J. Maier, K. Świerczek, *J. Solid State Chem.* **2022**, 306, 122731; c) J. E. Millburn, M. A. Green, D. A. Neumann, M. J. Rosseinsky, *J. Solid State Chem.* **1999**, 145, 401.
- [19] J. Ma, Y. Pan, Y. Wang, Y. Chen, *J. Power Sources* **2021**, 509, 230369.
- [20] R. P. Forslund, W. G. Hardin, X. Rong, A. M. Abakumov, D. Filimonov, C. T. Alexander, J. T. Mefford, H. Iyer, A. M. Kolpak, K. P. Johnston, K. J. Stevenson, *Nat. Commun.* **2018**, 9, 3150.
- [21] L. Zhang, F. Yao, J. Meng, W. Zhang, H. Wang, X. Liu, J. Meng, H. Zhang, *J. Mater. Chem. A* **2019**, 7, 18558.
- [22] a) Y. Takeda, R. Kanno, M. Sakano, O. Yamamoto, M. Takano, Y. Bando, H. Akinaga, K. Takita, J. B. Goodenough, *Mater. Res. Bull.* **1990**, 25, 293; b) J. P. Tang, R. I. Dass, A. Manthiram, *Mater. Res. Bull.* **2000**, 35, 411.
- [23] R. Wang, H. Liu, K. Zhang, G. Zhang, H. Lan, J. Qu, *Chem. Eng. J.* **2021**, 404, 126795.
- [24] W. Xu, R. Lan, D. Du, J. Humphreys, M. Walker, Z. Wu, H. Wang, S. Tao, *Appl. Catal. B-Environ.* **2017**, 218, 470.
- [25] Y. Li, H. S. Pillai, T. Wang, S. Hwang, Y. Zhao, Z. Qiao, Q. Mu, S. Karakalos, M. Chen, J. Yang, D. Su, H. Xin, Y. Yan, G. Wu, *Energy Environ. Sci.* **2021**, 14, 1449.
- [26] Z.-F. Li, Y. Wang, G. G. Botte, *Electrochim. Acta* **2017**, 228, 351.
- [27] a) A. Yang, J. Wang, K. Su, W. Lei, X. Qiu, Y. Tang, *Chem.-Eur. J.* **2021**, 27, 4869; b) L. A. Diaz, A. Valenzuela-Muñoz, M. Muthuvel, G. G. Botte, *Electrochim. Acta* **2013**, 89, 413.
- [28] Y. Zhu, H. A. Tahini, Z. Hu, J. Dai, Y. Chen, H. Sun, W. Zhou, M. Liu, S. C. Smith, H. Wang, Z. Shao, *Nat. Commun.* **2019**, 10, 149.
- [29] Y.-Y. Ma, C.-X. Wu, X.-J. Feng, H.-Q. Tan, L.-K. Yan, Y. Liu, Z.-H. Kang, E.-B. Wang, Y.-G. Li, *Energy Environ. Sci.* **2017**, 10, 788.
- [30] R. M. Choueiri, S. W. Tatarchuk, A. Klinkova, L. D. Chen, *Electrochim. Sci. Adv.* **2021**, 2100142.
- [31] R. Palaniappan, G. G. Botte, *J. Phys. Chem. C* **2013**, 117, 17429.
- [32] a) S. He, P. Hou, E. Petropoulos, Y. Feng, Y. Yu, L. Xue, L. Yang, *Front. Chem.* **2018**, 6, 219; b) H. Sakar, I. Celik, C. Balçık-Canbolat, B. Keskinler, A. Karagunduz, *J. Clean Prod.* **2019**, 215, 1415; c) P. B. Patil, V. M. Bhandari, V. V. Ranade, *Ultrason. Sonochem.* **2021**, 70, 105306; d) N. Yang, G. Zhan, D. Li, X. He, Y. Zhang, Q. Jiang, H. Liu, C. Wang, *Chem. Eng. J.* **2018**, 348, 271; e) J. Zhao, X. Wang, X. Li, S. Jia, Y. Peng, *Chem. Eng. J.* **2018**, 354, 589; f) B. Ye, T. Liang, Z. Nong, C. Qin, S. Lin, W. Lin, H. Liu, H. Li, *Desalination* **2021**, 520, 115372; g) G. Zhang, Y. Zhou, F. Yang, *Electrochim. Acta* **2019**, 299, 672.
- [33] L. Li, J. Yao, X. Fang, Y. Huang, Y. Mu, *Sci. Rep.* **2017**, 7, 41030.
- [34] Y.-J. Shih, S.-H. Huang, C.-L. Chen, C.-D. Dong, C.-P. Huang, *Electrochim. Acta* **2020**, 360, 136990.
- [35] F. Almomani, R. Bhosale, M. Khraisheh, A. Kumar, M. Tawalbeh, *Int. J. Hydrog. Energy* **2020**, 45, 10398.
- [36] W. Guan, S. Tian, D. Cao, Y. Chen, X. Zhao, *Electrochim. Acta* **2017**, 246, 1230.
- [37] H. Huang, P. Zhang, Z. Zhang, J. Liu, J. Xiao, F. Gao, *J. Clean Prod.* **2016**, 127, 302.
- [38] M. Panizza, C. A. Martinez-Huitle, *Chemosphere* **2013**, 90, 1455.
- [39] Y. Liu, L. Li, R. Goel, *J. Hazard. Mater.* **2009**, 167, 959.
- [40] D. Lee, H. N. Lee, *Materials* **2017**, 10, 368.
- [41] a) S. S. Pramana, A. Cavallaro, C. Li, A. D. Handoko, K. W. Chan, R. J. Walker, A. Regoutz, J. S. Herrin, B. S. Yeo, D. J. Payne, J. A. Kilner, M. P. Ryan, S. J. Skinner, *J. Mater. Chem. A* **2018**, 6, 5335; b) Y. Ling, T. Guo, Y. Guo, Y. Yang, Y. Tian, X. Wang, X. Ou, P. Feng, *J. Adv. Ceram.* **2021**, 10, 1052.
- [42] Q. He, K. Yao, X. Wang, X. Xia, S. Leng, F. Li, *ACS Appl. Mater. Interfaces* **2017**, 9, 41887.

- [43] Y.-P. Wang, Q. Xu, D.-P. Huang, K. Zhao, M. Chen, B.-H. Kim, *Int. J. Hydrog. Energy* **2017**, *42*, 6290.
- [44] H. Kim, C. Lim, O. Kwon, J. Oh, M. T. Curnan, H. Y. Jeong, S. Choi, J. W. Han, G. Kim, *Nat. Commun.* **2021**, *12*, 6814.
- [45] X. Jiang, D. Ying, X. Liu, M. Liu, S. Zhou, C. Guo, G. Zhao, Y. Wang, J. Jia, *Electrochim. Acta* **2020**, *345*, 136157.
- [46] J. Hu, S. Li, Y. Li, J. Wang, Y. Du, Z. Li, X. Han, J. Sun, P. Xu, *J. Mater. Chem. A* **2020**, *8*, 23323.
- [47] a) S.-Q. Liu, H.-R. Wen, G. Ying, Y.-W. Zhu, X.-Z. Fu, R. Sun, C.-P. Wong, *Nano Energy* **2018**, *44*, 7; b) Z. Zhang, Y. Jiang, X. Zheng, X. Sun, Y. Guo, *New J. Chem.* **2018**, *42*, 11285.
- [48] a) J. Hong, S. J. Heo, P. Singh, *Sci. Rep.* **2021**, *11*, 3368; b) S. Ni, X. Yang, T. Li, *Mater. Lett.* **2011**, *65*, 766.
- [49] X. Wang, Z. Li, Y. Qu, T. Yuan, W. Wang, Y. Wu, Y. Li, *Chem* **2019**, *5*, 1486.
- [50] M. Cao, X. Wu, X. He, C. Hu, *Langmuir* **2005**, *21*, 6093.
- [51] M. F. Sunding, K. Hadidi, S. Diplas, O. M. Løvvik, T. E. Norby, A. E. Gunnæs, *J. Electron Spectrosc. Relat. Phenom.* **2011**, *184*, 399.
- [52] Y.-J. Shih, Y.-H. Huang, C. P. Huang, *Electrochim. Acta* **2018**, *263*, 261.
- [53] S. Liu, C. Sun, J. Chen, J. Xiao, J.-L. Luo, *ACS Catal.* **2020**, *10*, 13437.
- [54] S. R. Choi, J.-I. Lee, H. Park, S. W. Lee, D. Y. Kim, W. Y. An, J. H. Kim, J. Kim, H.-S. Cho, J.-Y. Park, *Chem. Eng. J.* **2021**, *409*, 128226.
- [55] M. H. M. T. Assumpção, S. G. da Silva, R. F. B. de Souza, G. S. Buzzo, E. V. Spinacé, A. O. Neto, J. C. M. Silva, *Int. J. Hydrog. Energy* **2014**, *39*, 5148.
- [56] C. T. G. Petit, R. Lan, P. I. Cowin, J. T. S. Irvine, S. Tao, *J. Mater. Chem.* **2011**, *21*, 525.